Magnetic-field-induced sum-frequency mixing in sodium vapor

Alistair J. Poustie* and Malcolm H. Dunn†
J.F. Allen Physics Research Laboratories, Department of Physics and Astronomy, University of St. Andrews, North Haugh, St. Andrews, Fife, KY16 9SS, United Kingdom
(Received 31 July 1992)

An experimental and theoretical study of magnetic-field-induced sum-frequency mixing in sodium vapor has been carried out using two single-frequency, continuous-wave dye lasers as the sources of the fundamental radiation. In addition to the usual two-photon resonant enhancement of the three-wave-mixing nonlinear-optical process, the use of near- or on-resonant single-photon transitions for further resonant enhancement was investigated. The macroscopic phase-matching behavior of the sum-frequency mixing was examined with the intermediate states off resonance. Experimental and theoretical results are presented to illustrate the differences that occur between the coherent quadrupole emission and the incoherent cascade fluorescence when the intermediate states in the two-photon absorption are resonant. Control over the single-photon resonant enhancement and the sum-frequency-mixing phase matching was achieved to increase the power conversion efficiency to 1.2×10^{-5}.

PACS number(s): 42.65.Ky, 32.80.Wr

I. INTRODUCTION

A normally isotropic atomic vapor can be used as a nonlinear medium for second-order nonlinear-optical processes if some technique is used to break the symmetry of the vapor [1]. This has previously been achieved by using an external transverse electric [2–9] or magnetic field [10–20] applied to the vapor, excitation with high-power laser pulses [12,21–29], or by using a noncollinear beam geometry [11,13,30–33]. We have used a transverse dc magnetic field to remove the isotropy and have studied high-resolution, collinear sum-frequency mixing (SFM) in sodium vapor with the nonlinear process resonantly enhanced by both single- and two-photon transitions in the sodium atom. Figure 1 shows the excitation scheme, the sodium energy levels which are utilized for resonant enhancement, and the wavelengths of interest.

Previous reports of magnetic-field-induced three-wave mixing have concentrated on second-harmonic generation (SHG) [12,15,17–20], although SFM [11,13,14] and difference-frequency mixing (DFM) [10] have also been demonstrated. Generally in these processes, a resonant two-photon absorption in the atom creates coherent quadrupole moments that oscillate at the sum or difference frequency but these radiate perpendicularly to the beam propagation direction and power is not transferred to the sum- or difference-frequency wave. The transverse magnetic field splits the magnetic sublevels of the atomic levels via the Zeeman effect and rotates the quadrupole moments to allow collinear generation of the second-harmonic, sum-frequency, or difference-frequency beam. The magnetic-field-induced SHG process in sodium vapor has been studied in detail by Sinclair and Dunn [19,20]. They were able to examine the influence of atomic selection rules and line-broadening processes on the nonlinear-optical effect by using an atomic vapor as the nonlinear medium and continuous-wave (cw) single-frequency laser excitation, which allowed the microscopic properties of the SHG process to be investigated with well-defined laser and atomic parameters.

We extend their work here to examine SFM and the role of the resonant or near-resonant $3P$ intermediate states in the $3S$-$4D$ two-photon absorption and in the parametric emission. We utilize additional single-photon resonant enhancement to increase the magnitude of the effective second-order nonlinear coefficient in the sodium vapor. The advantage of increasing the two-photon absorption cross section through single-photon as well as two-photon resonant enhancement was experimentally studied by Bjorkholm and Liao in the early investigations of two-photon spectroscopy [34]. They showed that when the laser frequencies were also tuned close to single-photon resonance, an increase in the two-photon cross section of over seven orders of magnitude could be obtained compared to degenerate frequency excitation [35]. With the $3P$ sodium states exactly on resonance, the two-photon spectroscopic line intensities were over 10^9

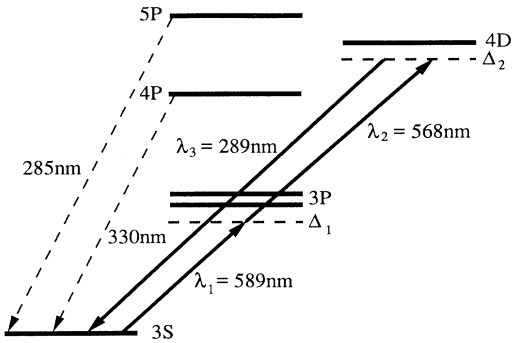

FIG. 1. Schematic diagram of the sodium energy levels of interest for the SFM study. The fundamental visible optical waves are at wavelengths $\lambda_{1,2}$ and the generated ultraviolet wave is at wavelength λ_3. Cascade fluorescence from the $4P$ and $5P$ states is used to monitor the atomic population.

times larger than for equal-frequency two-photon excitation [36]. With resonant intermediate states either copropagating or counterpropagating beams could be used for excitation with no loss of resolution in the spectrum. This on-resonance two-photon spectroscopic technique subsequently allowed weak transitions to be probed [37] and detailed collisional effects to be measured [38,39]. For magnetic-field-induced SFM, however, the advantage of obtaining a large $\chi^{(2)}$ second-order susceptibility through additional single-photon resonant enhancement is offset against the requirement to phase-match the nonlinear-optical process. The refractive index of the sodium vapor becomes significant even at low particle densities when one of the fundamental laser frequencies is tuned close to single-photon resonance and this dispersion determines the SFM phase-matching behavior and overall power conversion efficiency.

In Sec. II we develop a semiclassical cascade three-level atomic model to illustrate the important contribution of homogeneous atomic dispersion effects when the intermediate states in the two-photon absorption are resonant. The model also predicts the microscopic response of the coherent SFM emission for this condition. In contrast to previous theoretical treatments of two-photon absorption [40–43] or coupled Doppler-broadened transitions [44,45], it is the *coherence* between the final- and ground-state atomic levels which drives the quadrupole moments that is mainly of interest here, rather than the final-state population which provides the spectroscopic information.

The experimental results for magnetic-field-induced SFM with the intermediate states either nonresonant or resonant are presented in Sec. III. We examined both the microscopic and macroscopic behavior of the SFM, although the two are connected when the intermediate states are resonant. For this case, the experimental results are compared with features of the three-level atomic model and we also discuss the effects of velocity-selective excitation, optical pumping, and saturation, which play a significant role in the magnetic-field-induced SFM process.

II. THEORY

Although the semiclassical model of a cascade three-level atomic system interacting with two resonant light fields has been considered before in connection with two-photon spectroscopy [40–43], we briefly discuss the model to predict the behavior of the magnetic-field-induced SFM in this atomic system. We consider the situation shown in Fig. 2, where copropagating laser beams of frequencies ω_1 and ω_2 interact with a three-level atom with a ground state $|1\rangle$ of energy $\mathcal{E}_1$, an intermediate state $|2\rangle$ of energy $\mathcal{E}_2$, and a final state $|3\rangle$ of energy $\mathcal{E}_3$. The laser beams have electric fields described by

$$E_j(z,t)=\tfrac{1}{2}(E_0)_j\exp[i(\omega_j t-k_j z)]+\text{c.c.} , \tag{1}$$

where $j=1,2$ and $\omega_1\neq\omega_2$. The laser beams must propagate in the same direction since the SFM phase-matching condition $\mathbf{k}_3=\mathbf{k}_1+\mathbf{k}_2$ is difficult to satisfy for counterpropagating beams. The atomic levels are connected by the

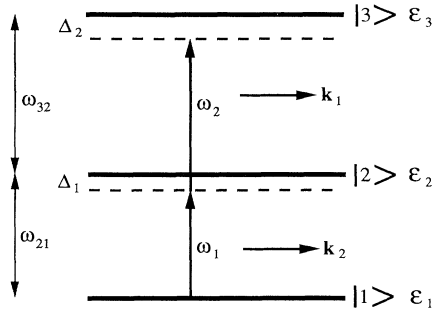

FIG. 2. Schematic three-level atomic system used for the theoretical model.

dipole matrix elements.

$$\begin{aligned}&\langle 1|\mu|2\rangle\equiv\mu_{12}\neq 0 ,\\ &\langle 2|\mu|3\rangle\equiv\mu_{23}\neq 0 ,\\ &\langle 1|\mu|3\rangle=0 ,\end{aligned} \tag{2}$$

where μ is the dipole operator. There is a quadrupole coupling but no dipole coupling between the final and ground states and the weak quadrupole matrix element is assumed here to be negligible. The Rabi frequencies for the two dipole transitions are defined by

$$\alpha=\frac{\mu_{12}E_1}{\hbar} \tag{3}$$

and

$$\beta=\frac{\mu_{23}E_2}{\hbar} . \tag{4}$$

The atomic transition frequencies are given by

$$\Omega_{ij}=(\mathcal{E}_j-\mathcal{E}_i)/\hbar , \tag{5}$$

where $\Omega_{12}<\Omega_{23}$. The frequencies of the two light fields are chosen so that $\omega_1\approx\Omega_{12}$, $\omega_2\approx\Omega_{23}$, and $\omega_1+\omega_2\approx\Omega_{13}$. This ensures that each light field only interacts with one of the dipole transitions and that only the sum frequency can excite the two-photon resonance. The exact detunings of ω_1 from single-photon resonance and $\omega_1+\omega_2$ from two-photon resonance are given by

$$\Delta_1=\Omega_{12}-\omega_1+k_1 v_z \tag{6}$$

and

$$\Delta_2=\Omega_{13}-(\omega_1+\omega_2)+(k_1+k_2)v_z , \tag{7}$$

respectively, where v_z is the velocity of a particular homogeneous atomic group viewed along the light-propagation direction $\hat{\mathbf{z}}$. These velocity-selective detunings account for the inhomogeneous Doppler broadening of the optical transitions.

A density-matrix treatment of this system, which is valid in all powers of the amplitudes of the two applied fields and includes all saturation effects, can be used [46]. This is necessary for a model of magnetic-field-induced SFM since, in general, the optical-field strengths will

exceed the saturation intensities of the atomic dipole transitions when the intermediate state is resonant. The time development of the density matrix ρ is given by [47]

$$i\hbar\dot{\rho}=[H,\rho]-\Gamma(\rho-\rho_0) , \tag{8}$$

where Γ represents the relaxation processes and the Hamiltonian H is composed of the free-atom Hamiltonian H_0, which can include the effect of the external magnetic field, and the electric dipole Hamiltonian H_I,

$$H_I=-\boldsymbol{\mu}\cdot\mathbf{E}(z,t) , \tag{9}$$

where μ is the dipole moment of the atomic transition. The oscillations of the density-matrix components at optical frequencies are removed by transforming the off-diagonal elements ρ_{ij} to the slowly varying operators $\tilde{\rho}_{ij}$, where

$$\begin{aligned}\rho_{12}&=\tilde{\rho}_{12}\exp[i(\omega_1 t+k_1 z)] ,\\ \rho_{23}&=\tilde{\rho}_{23}\exp[i(\omega_2 t+k_2 z)] ,\\ \rho_{13}&=\tilde{\rho}_{13}\exp[i(\omega_1+\omega_2)t+(k_1+k_2)z] .\end{aligned} \tag{10}$$

Solving the time-dependent equation for the slowly varying operators $\tilde{\rho}$ and using the rotating-wave approximation to remove rapidly oscillating terms gives the system of density-matrix equations

$$\dot{\rho}_{11}=i\alpha(\tilde{\rho}_{21}-\tilde{\rho}_{12})-\Gamma_{11}(\rho_{11}-\rho_{11}^0) , \tag{11a}$$

$$\dot{\rho}_{22}=i\alpha(\tilde{\rho}_{12}-\tilde{\rho}_{21})+i\beta(\tilde{\rho}_{32}-\tilde{\rho}_{23})-\Gamma_{22}(\rho_{22}-\rho_{22}^0) , \tag{11b}$$

$$\dot{\rho}_{33}=i\beta(\tilde{\rho}_{12}-\tilde{\rho}_{32})-\Gamma_{33}(\rho_{33}-\rho_{33}^0) , \tag{11c}$$

$$\dot{\tilde{\rho}}_{12}=-i(\Delta_1-i\Gamma_{12})\tilde{\rho}_{12}+i\alpha(\rho_{22}-\rho_{11})-i\beta\tilde{\rho}_{13} , \tag{11d}$$

$$\dot{\tilde{\rho}}_{23}=-i(\Delta_2-\Delta_1-i\Gamma_{23})\tilde{\rho}_{23}+i\beta(\rho_{33}-\rho_{22})+i\alpha\tilde{\rho}_{13} , \tag{11e}$$

$$\dot{\tilde{\rho}}_{13}=-i(\Delta_2-i\Gamma_{13})\tilde{\rho}_{13}-i\beta\tilde{\rho}_{12}+i\alpha\tilde{\rho}_{23} . \tag{11f}$$

The terms ρ_{ii}^0 represent the population of the atomic levels under thermal equilibrium and in the absence of the applied light fields. For moderate temperatures and optical atomic transition frequencies, the thermal populations are

$$\rho_{11}^0=1, \quad \rho_{22}^0=\rho_{33}^0=0 . \tag{12}$$

Population can be conserved in the three-level model by defining

$$\rho_{11}+\rho_{22}+\rho_{33}=1 \tag{13}$$

and the relaxation rates of the off-diagonal elements are given by

$$\Gamma_{ij}=\tfrac{1}{2}(\Gamma_{ii}+\Gamma_{jj}) , \tag{14}$$

where Γ_{ii} and Γ_{jj} are the decay rates for the atomic population in states $|i\rangle$ and $|j\rangle$. This assumes that the phase-disturbing collisions are weak [48]. The degree of single-photon saturation produced by the optical fields is

$$\frac{I}{I_{\text{sat}}}=\frac{4\Lambda^2}{\Gamma_{ii}\Gamma_{ij}} , \tag{15}$$

where I is the optical intensity, I_{sat} is the saturation intensity, and Λ is one of the single-photon transition Rabi frequencies as defined in (3) and (4).

The steady-state solutions to the density-matrix equations, which are required for calculating the response of the atom under cw laser excitation, are found by setting all of the time derivatives equal to zero. Analytical solutions to the steady-state equations have previously been derived [40] but the complexity of the solutions is such that little physical insight is gained from them [46]. We chose to numerically solve the steady-state density-matrix equations and included Doppler broadening by integrating the solutions over the usual Maxwellian velocity distribution

$$f(v_z)=(M/2\pi k_B T)^{1/2}\exp(-Mv_z^2/2k_B T) , \tag{16}$$

where M is the atomic mass, T is the absolute temperature, and k_B is Boltzmann's constant. The numerical values for the relaxation rates, Rabi frequencies, and laser detunings were chosen so that the parameters appropriate to the SFM experimental conditions could be used in the calculations.

The quantities of interest in this three-level model are not only the induced coherence $|\rho_{13}|^2$ between the final and ground states which drives the quadrupole moment for coherent SFM emission, but also the refractive index experienced by the interacting waves in the atomic vapor which influences the phase matching of the nonlinear-optical-mixing effect. The refractive index for the sum-frequency wave is assumed to be constant and equal to unity since the quadrupole transitions are weak and the wavelength is far from any single-photon transitions in the sodium atom. However, there are significant contributions to the refractive indices for the two fundamental waves when the intermediate states are resonant or near resonant. These can be expressed in the form $n(\omega)\approx 1+\chi'(\omega)/2$ as [47]

$$n(\omega_1)\approx 1+\frac{\Delta N_{12}\mu_{12}^2\text{Re}\rho_{12}}{2\varepsilon_0\hbar\alpha} , \tag{17}$$

$$n(\omega_2)\approx 1+\frac{\Delta N_{23}\mu_{23}^2\text{Re}\rho_{23}}{2\varepsilon_0\hbar\beta} , \tag{18}$$

where ΔN_{ij} is the atomic-population difference between atomic levels i and j.

We give two examples of typical numerical solutions to the density-matrix equations to illustrate the important differences that occur for the SFM nonlinear effect when the intermediate state is off and on resonance.

a. Intermediate state off resonance. This is the condition for magnetic-field-induced SHG and usually also for two-photon spectroscopy. Figure 3 shows the calculated density-matrix elements for laser frequency ω_1 held at a fixed detuning of 10 GHz from the ground-to-intermediate-state single-photon resonance, outside the single-photon Doppler width of ≈ 1.5 GHz, and as laser frequency ω_2 is tuned through the two-photon resonance.

As expected, the final-state population line shape is also Doppler broadened, since the two laser beams are copropagating, and has a half width of ≈ 3.5 GHz due to the combined inhomogeneous widths of the ground and final atomic states. The intermediate state has essentially no influence on the resolved width of the two-photon resonance. The final-ground-state coherence has a similar Doppler-broadened width due to all homogeneous atomic velocity groups being equally excited by the two-photon absorption, which is in agreement with the experimental SFM and SHG results. Figure 3 also shows that there is a small but well-defined inhomogeneous refractive index change for the beam at frequency ω_2 due to the induced two-photon absorption [49,50].

b. Intermediate state on resonance. Bringing the intermediate state on resonance significantly alters the behavior of the atomic system to the applied light fields. This is shown in Fig. 4 for the case where laser frequency ω_1 is detuned 0.25 GHz from the center of the single-photon Doppler width so that real population is excited into the intermediate atomic level. This population mainly results from velocity-selective excitation of the particular homogeneous velocity group which is Doppler shifted to be exactly on resonance with ω_1. This is the well-known hole-

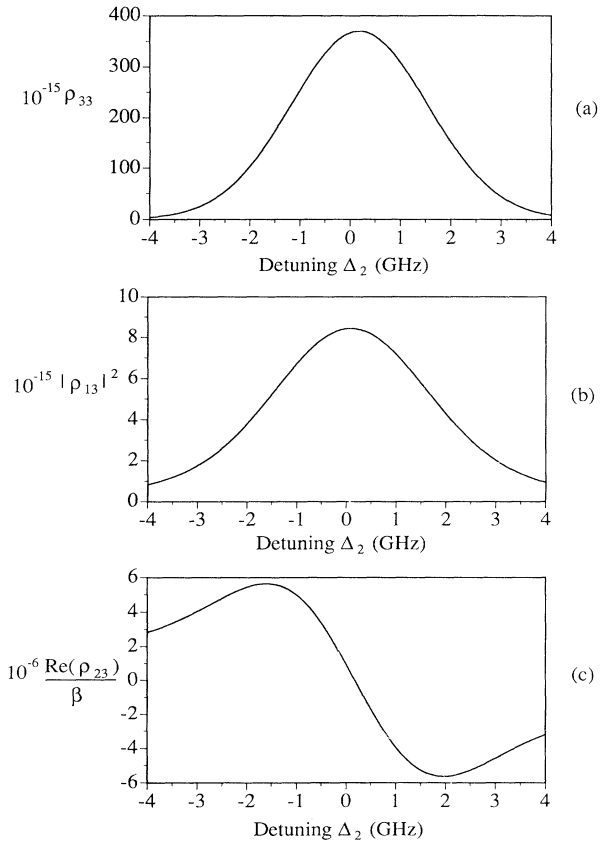

FIG. 3. Calculated variation of (a) the final-state population, (b) the final-ground-state atomic coherence, and (c) the refractive index for ω_2 with detuning from two-photon resonance. Intermediate state detuned by $\Delta_1=10$ GHz, $\alpha=0.001$, $\beta=0.001$, $\Gamma_{22}=0.02$, $\Gamma_{33}=0.05$, $T=423$ K.

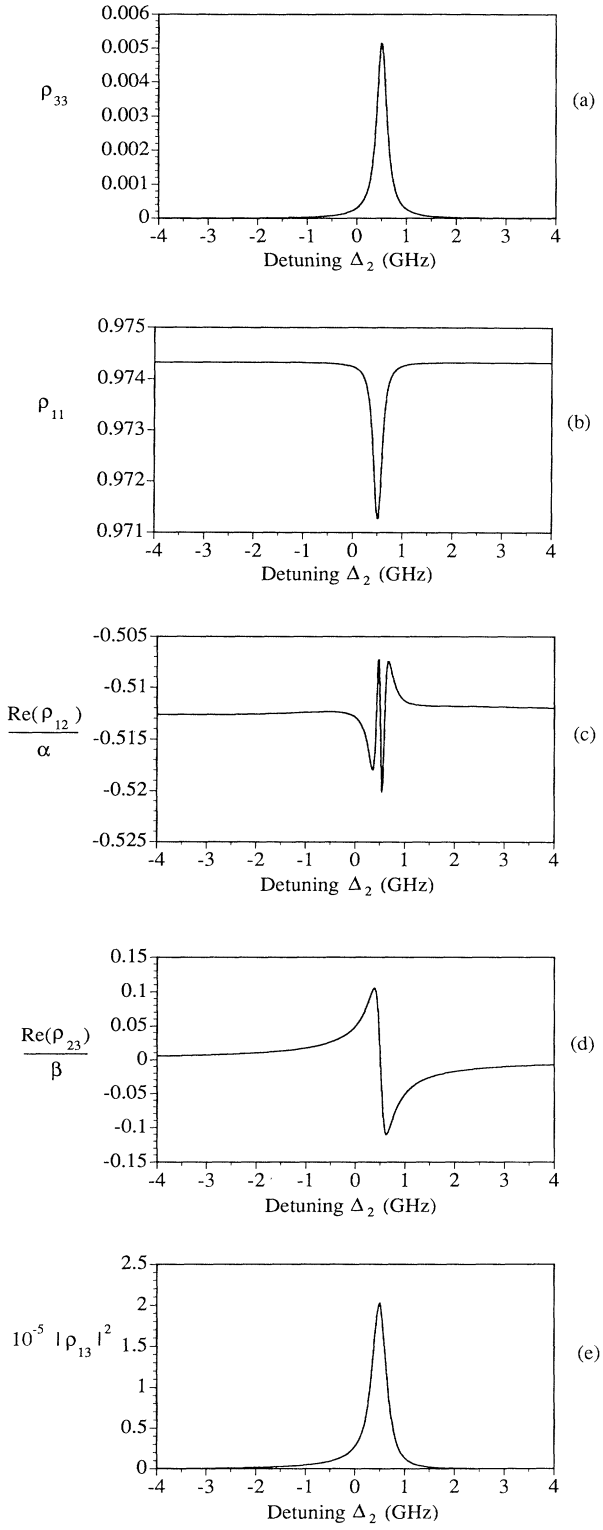

FIG. 4. Calculated variation of (a) the final-state population, (b) the ground-state population, (c) the refractive index for ω_1, (d) the refractive index for ω_2, and (e) the final-ground-state atomic coherence with detuning from two-photon resonance. Intermediate state detuned by $\Delta_1=0.25$ GHz, $\alpha=0.0224$, $\beta=0.028$, $\Gamma_{22}=0.02$, $\Gamma_{33}=0.05$, $T=423$ K.

burning effect in an inhomogeneously broadened transition [51]. The velocity selection produces a Lorentzian distribution of population in the intermediate level which influences the final-level population line shape as ω_2 is tuned to complete the two-photon resonance. The linewidth of the final-state population distribution is determined by the homogeneous linewidths of the intermediate and the final states, both of which are power broadened in this example due to the optical-field strengths being larger than the single- and two-photon saturation intensities. The absolute frequency of the two-photon resonance occurs at $\Delta_2 \approx 0.49$ GHz due to the residual Doppler shift of the excited homogeneous atomic group. These effects are fully discussed in Sec. III B, where the experimental magnetic-field-induced SFM results are presented.

The final-ground-state coherence also displays a Lorentzian line shape and is centered at the same two-photon resonant frequency as the population in the final level, indicating that the velocity-selected atomic group also provides the main contribution to the coherence. This result is interesting because it appears to contradict earlier theoretical work [52] in which this coherence term is also calculated and in which it is concluded that the coherence must vanish due to the velocity averaging over the inhomogeneous Doppler components. Our calculations and experimental SFM results oppose this previous conclusion that only DFM is possible in a coupled three-level atomic system.

Figure 4(b) also shows the modifications that occur in the ground-state population when $\omega_1+\omega_2$ is two-photon resonant due to excitation of velocity-selected population through the intermediate and final atomic levels. The ensuing refractive index variations for frequencies ω_1 and ω_2 are shown in Figs. 4(c) and 4(d). These narrow, frequency-dependent variations in the refractive index modify the overall phase-matching condition for the magnetic-field-induced SFM, which produces a modulation in the SFM power across the coherent line profile. To illustrate this, consider the phase mismatch Δk given by

$$\Delta k = k_3 - k_1 - k_2 \approx -2\pi \left[\frac{\Delta n(\omega_1)}{\lambda_1} + \frac{\Delta n(\omega_2)}{\lambda_2} \right] = \Delta k_1 + \Delta k_2 , \quad (19)$$

where $n = 1 + \Delta n$ is the refractive index as given in Eqs. (17) and (18). For collinear plane waves, the dependence of the generated SFM power on the phase mismatch is [53]

$$P(\omega_1+\omega_2) \propto \frac{L^2 \sin^2(\Delta k L/2)}{(\Delta k L/2)^2} , \quad (20)$$

where L is the effective interaction length for the nonlinear-optical effect. We assume that $\Delta k_1 L/2 \approx 3.0$ for our experimental interaction lengths and estimated refractive index for ω_1 in the sodium vapor when $\omega_1+\omega_2$ is not two-photon resonant. The additional phase mismatch produced by Δk_2 and further Δk_1 when $\omega_1+\omega_2$ is tuned through the two-photon resonance varies the generated SFM power according to Eq. (20). The product of the mismatch factor due to the refractive index changes and the magnitude of the coherence $|\rho_{13}|^2$ is proportional to the SFM power and is shown in Fig. 5, where an induced subhomogeneous dip is now apparent on the line profile. This feature does not appear on the incoherent final-level population ρ_{33} line profile since phase matching does not affect the atomic populations.

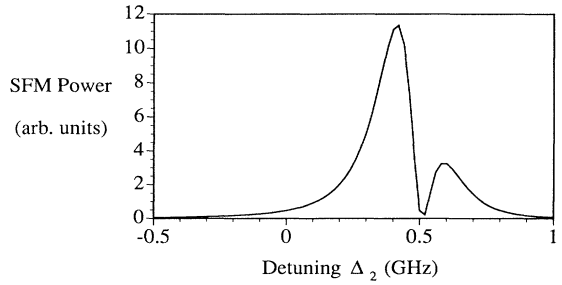

FIG. 5. Calculated final-ground-state atomic coherence including the effects of phase matching. Parameters are the same as for Fig. 4.

III. EXPERIMENT

Our experimental apparatus consisted of two cw single-mode frequency-stabilized ring dye lasers (Spectra-Physics 380D, Coherent 699-21) whose unfocused beams ($\approx$4-mm diameter) were combined and passed collinearly through a heat-pipe oven containing the sodium vapor and argon buffer gas. The effective interaction length defined by the vapor column was 10 cm. The oven was typically operated at a low temperature of $\approx 120-130\,^{\circ}\mathrm{C}$ and with buffer gas pressures of ≈ 1 mbar. Magnetic fields of up to 0.4 T could be applied transversely to the oven using an electromagnet which had 10-cm-long pole pieces. The 330-nm cascade fluorescence from the $4P$ states, which monitored the population excited into the $4D$ states, and the coherent SFM emission at 289 nm were detected with filtered photomultiplier tubes (Hamamatsu R212 and R166UH, respectively, with two Corning 9863 filters). A monochromator was used as a wavelength-selective filter when detecting the SFM radiation to discriminate against a strong fluorescent signal at 285 nm that was apparent on two-photon resonance when the intermediate $3P$ states were also resonant. We attributed this signal to collisional-induced population of the $5P$ sodium states from the laser-excited $4D$-state population, and subsequent spontaneous emission to the $3S$ ground states. The absolute frequency of the laser beam tuned close to the $3S$-$3P$ single-photon transitions was calibrated via saturated absorption spectroscopy in a separate sodium cell. The scan of the second laser beam through the two-photon-enhancing $4D$ states was calibrated by monitoring the transmission of a temperature-stabilized confocal interferometer with a free spectral range of 250 MHz. For most of the experiments, phase-sensitive detection was used to improve the single-to-noise ratio.

A. Intermediate states off resonance

1. Microscopic effects

As anticipated for this detuning case, the magnetic-field-induced SFM displayed microscopic behavior similar to that of magnetic-field-induced SHG. For each particular selection of ω_1 and ω_2, a coherent signal at 289.4 nm was only detected when $\omega_1+\omega_2$ was two-photon resonant with the sodium $3S$-$4D$ two-photon transition. The high-resolution line profiles were Doppler broadened and were subject to the same atomic selection rules as for SHG, although for SFM there was additional control over which of the coherent quadrupole moments was driven by correct choice of the laser polarizations and magnetic-field geometry. The magnitude of the SFM intensity increased linearly with P_1 and P_2, the powers of the beams at frequencies ω_1 and ω_2, respectively, as the square of the magnetic-field strength at low field strengths, and saturated at higher magnetic-field strengths of ≈ 0.1 T.

2. Macroscopic effects

The advantage of tuning ω_1 close to the single-photon $3S$-$3P$ transitions to increase the two-photon absorption cross section was offset by the requirement to phase-match the SFM nonlinear-mixing effect. The SFM macroscopic behavior differed from SHG due to the ability to select the vapor dispersion and phase mismatch with an appropriate choice of the two fundamental beam frequencies. The main contribution to the dispersion of the sodium vapor, which can be calculated using the Sellmeier equation [54], arises from the same $3S$-$3P$ single-photon transitions that provide the resonant enhancement. Figure 6 shows the calculated variation of the phase mismatch Δk for different values of λ_1 near the sodium $3S_{1/2}\rightarrow 3P_{1/2}$ D_1 line ($\lambda=589.6$ nm) and the $3S_{1/2}\rightarrow 3P_{3/2}$ D_2 line ($\lambda=589.0$ nm). In each case, the value of λ_2 is chosen to complete a two-photon transition to the sodium $4D$ states and λ_3 corresponding to the SFM emission is fixed at 289.4 nm. The dispersion experienced by the ultraviolet sum-frequency wave is negligible compared to that for the two visible fundamental wavelengths. Note that the magnitude of the phase mismatch rapidly increases as ω_1 approaches one of the D-line transitions.

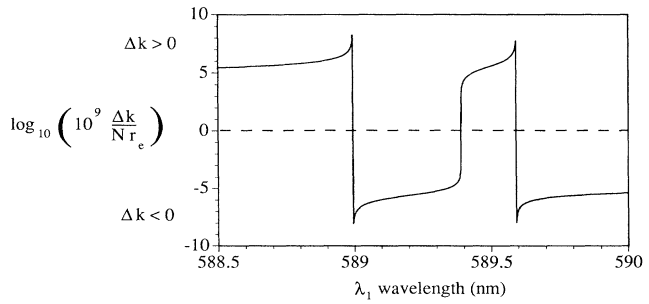

FIG. 6. Calculated variation of the phase mismatch Δk with wavelength near the sodium D lines. N is the atomic density and r_e is the classical electron radius.

The measured variation of total SFM power with the sodium density initially increased as the square of the atomic density and then showed the same oscillatory variation as for SHG. The phase-match peaks shifted to progressively lower sodium densities as ω_1 was tuned closer to the single-photon transitions and as the coherence length in the vapor became shorter. However, there is also a zero in the phase-mismatch values at $\lambda_1\approx 589.4$ nm due to a cancellation of the refractive index contributions from the D_1 and D_2 single-photon transitions. At this wavelength, the sodium vapor is also nonabsorbing. We utilized the lack of absorption and the cancellation in the dispersion to achieve nominal phase matching with $\Delta k=0$ and observed a continual increase in the SFM power with sodium vapor temperature up to the maximum temperature that could be obtained, as shown in Fig. 7. The use of anomalous dispersion to achieve phase matching in a vapor was originally suggested by Armstrong *et al.* [55] and has been utilized before in four-wave mixing studies [54,56,57].

The choice of ω_1 not only allows the magnitude of the phase mismatch to be selected but also allows the sign of Δk to be chosen. This can be of benefit because alternative techniques of phase matching such as using a buffer gas [58] or noncollinear beams [13] become possible when $\Delta k<0$. The use of buffer gas to phase-match magnetic-field-induced SFM is limited because the process is two-photon resonant and the $3S$-$4D$ coherence is damped by the phase-disturbing collisions between the sodium and the buffer gas atoms.

Experimentally, variations were observed in the SFM phase-matching behavior when the input Gaussian beams were focused into the oven due to the phase variation that occurs in passing through the focus [59,60]. When $\Delta k>0$, the SFM power was oscillatory with increasing sodium vapor density and the densities corresponding to the peaks and troughs of the phase-matching behavior agreed well with theory, as shown in Fig. 8. The magnitude of the peaks tended to decrease with increasing atomic density for some particular values of ω_1, which

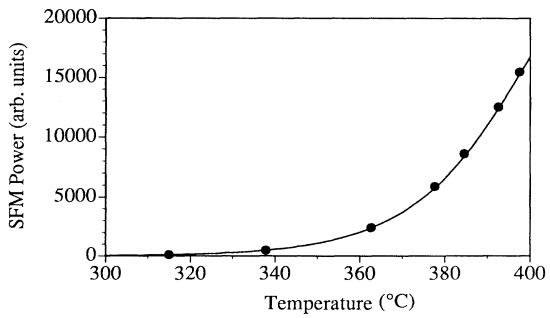

FIG. 7. Measured (points) and calculated (line) variation in SFM power with sodium vapor temperature. Magnetic-field strength $=0.004$ T, $\lambda_1=589.388$ nm (polarization perpendicular to the magnetic-field direction), $\lambda_2=568.458$ nm (polarization parallel to the magnetic-field direction), confocal parameter of laser beams equal to the interaction length.

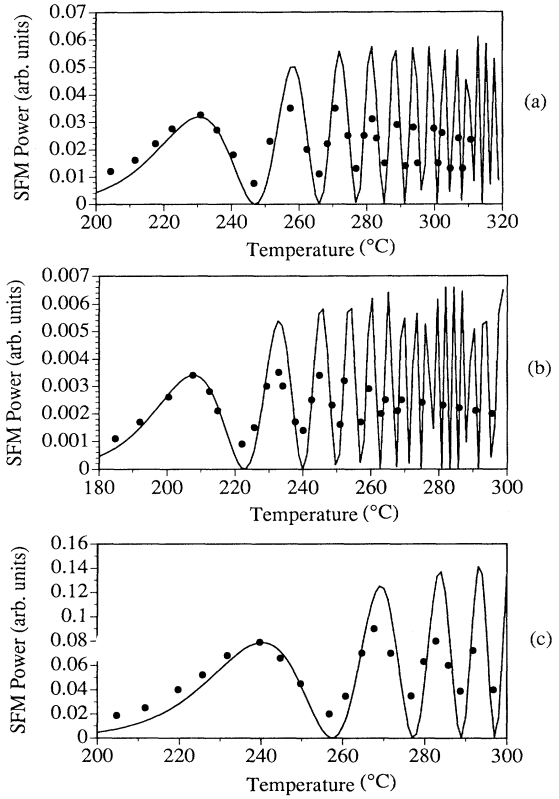

FIG. 8. Measured (points) and calculated (line) variation in SFM power with sodium vapor temperature. Magnetic-field strength =0.1 T, confocal parameter of beams equal to the interaction length, laser polarizations relative to magnetic-field direction as in Fig. 7. (a) $\lambda_1=588.790$ nm, $\lambda_2=569.016$ nm, (b) $\lambda_1=588.933$ nm, $\lambda_2=568.882$ nm, (c) $\lambda_1=589.500$ nm, $\lambda_2=568.354$ nm.

was probably due to increased sodium dimer absorption for the fundamental beams. When $\Delta k<0$, the SFM power displayed one large peak as a function of sodium density that was several times the magnitude of the oscillations for $\Delta k>0$, as predicted by the theory. The absolute sodium density corresponding to the experimentally measured main peak in the SFM power did not generally agree with the expected theoretical value, as shown in Fig. 9. We were able to account for this by including an additional phase mismatch that resulted from a slight residual noncollinearity in the alignment of the two focused fundamental beams [30,13]. In Fig. 9 the required angle between the beams to match the theory to the experimental result was calculated to be $\Theta\approx 14$ mrad. Other experimental measurements with different laser wavelengths or different beam angles to change the contribution of the additional phase mismatch were consistent with this explanation of the beam noncollinearity producing the apparent disagreement between collinear theory and experiment.

In general, the advantage of utilizing anomalous dispersion to phase-match the magnetic-field-induced SFM nonlinear-optical process is that it should allow the

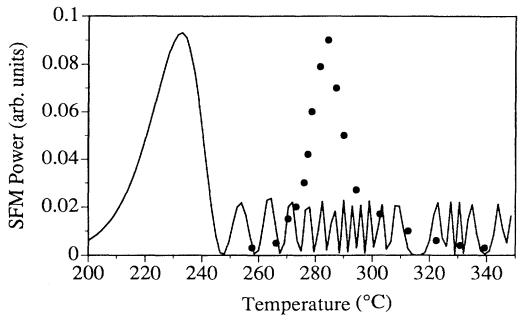

FIG. 9. Measured (points) and calculated (line) variation in SFM power with sodium vapor temperature for $\Delta k<0$. Magnetic-field strength =0.075 T, confocal parameter of beams equal to the interaction length, $\lambda_1=589.090$ nm, $\lambda_2=568.736$ nm, laser polarizations relative to magnetic-field direction as in Fig. 7.

optimum phase-mismatch value to be chosen for any interaction lengths, vapor densities, and laser beam focusing parameters by the appropriate choice of the input wavelengths.

B. Intermediate states on resonance

When the intermediate states in the two-photon excitation are brought on resonance, several considerations are introduced in the microscopic and macroscopic behavior of the magnetic-field-induced SFM nonlinear-optical process. Tuning ω_1 and ω_2 within the Doppler widths of the $3S$-$3P$ and $3P$-$4D$ single-photon transitions couples the two atomic transitions and allows significant light-induced population changes to occur within the three levels. These population changes can be homogeneous due to hole burning and velocity-selective excitation or inhomogeneous due to optical-pumping effects in the atomic ground state. The corresponding refractive index variations in the atomic vapor determine the phase matching of the SFM process and the overall output power. For these experiments the laser beams were unfocused ($\approx$4-mm diameter) to minimize any phase-shifting effects of the Gaussian beams and to reduce the effects of higher-order nonlinear-optical effects. The effects of velocity selection, optical pumping, single- and two-photon saturation, and frequency-dependent phase matching on magnetic-field-induced SFM are now considered in detail.

1. Velocity-selective excitation

When the laser frequency ω_1 lies within the $3S$-$3P$ Doppler width and is detuned by Δ_1 from line center, the particular homogeneous group with velocity $v=2\pi\Delta_1/k_1$ which is Doppler shifted exactly on resonance with ω_1 will be preferentially excited. The subsequent excitation of this group to the final state by the copropagating beam of frequency ω_2 then produces a narrow Lorentzian homogeneous population distribution in the final state with a corresponding linewidth [full width at half maximum (FWHM)] of

$$\Delta\omega_3 + |(\omega_1+\omega_2)/\Omega_{12}|\Delta\omega_2 , \quad (21)$$

where $\Delta\omega_2$ and $\Delta\omega_3$ are the homogeneous linewidths of the intermediate and final states, respectively. These linewidths may have contributions from power and collisional broadening in addition to spontaneous emission. The absolute frequency of ω_2 to achieve two-photon resonance depends on the relative Doppler shift of the initially excited homogeneous group. This results in any ground-state atomic structure with splitting $\delta\omega_g$ appearing as $(\omega_2/\omega_1)\delta\omega_g$ in the two-photon absorption spectrum. Similarly, the on-resonance two-photon excitation is also sensitive to structure in the intermediate atomic state and produces splittings of $\delta\omega_i(\omega_1+\omega_2)/\omega_1$. These velocity-selective effects are shown in Fig. 10, which is an experimental two-photon line profile of the cascade fluorescence at 330 nm when ω_1 is resonant with the sodium D_1 line. The four observed lines correspond to two-photon transitions from the two hyperfine levels of the $3S$ ground state to the single $4D_{3/2}$ final state via the two hyperfine levels of the $3P_{1/2}$ intermediate state. The observed splittings agree well with the theoretical splittings of $a\rightarrow c = b\rightarrow d = (\nu_2/\nu_1)\delta\nu_g = (1.038)(1772)$ MHz $= 1839$ MHz and $a\rightarrow b = c\rightarrow d = \delta\nu_i(\nu_1+\nu_2)/\nu_1 = (2.038)(190)$ MHz $= 387$ MHz. Note that the resonance linewidths are collisionally and power broadened due to buffer gas collisions and laser intensities of several times the single-photon saturation intensities. The magnitude of the homogeneous line dominates over any Doppler-broadened excitation when ω_1 lies within the single-photon Doppler width [46] and the background inhomogeneous signal apparent in Fig. 10 arises due to velocity-changing collisions thermalizing the initially homogeneous velocity selection and collisional redistribution [38,39].

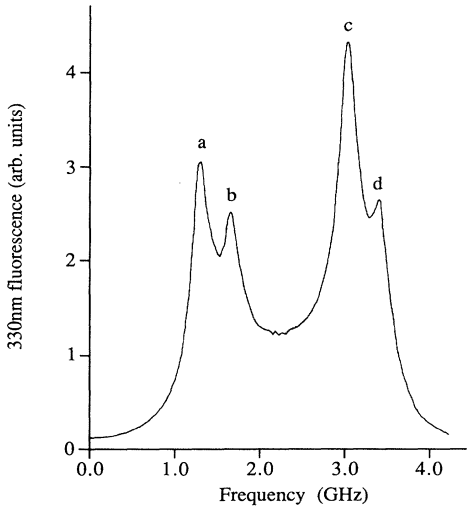

FIG. 10. Experimental two-photon spectrum of the sodium $3S$-$4D$ transition using the $3P_{1/2}$ state as the resonant intermediate state. No magnetic field applied, 1 mbar argon buffer gas, vapor temperature $= 393$ K, $I_1 = 400$ mW cm^{-2}, $I_2 = 800$ mW cm^{-2}. Laser frequency ν_1 tuned midway between the $3S_{1/2}(F=1)\rightarrow 3P_{1/2}$ and $3S_{1/2}(F=2)\rightarrow 3P_{1/2}$ single-photon transition frequencies.

2. *Optical pumping*

In addition to these hole-burning effects, the use of on-resonance single-photon transitions in the two-photon absorption can induce large changes in the ground-state hyperfine population distributions by optical pumping [61]. These ground-state population changes are detrimental to the magnetic-field-induced SFM process due to the significant associated refractive index variations for the beam at frequency ω_1 which produce phase mismatching. For example, if ω_1 is tuned midway between the single-photon transitions from the $F=1$ and $F=2$ hyperfine ground states to a $3P$ state, then the refractive index contribution can be approximately four times larger if all the population is pumped into the $F=2$ sublevel as opposed to an equal population distribution in the ground states.

We experimentally determined the population redistribution produced by a relatively strong laser beam (≈ 0.5 W cm^{-2}) on resonance within the $3S_{1/2}\rightarrow 3P_{3/2}$ transition Doppler width, which was typical for the on-resonance SFM experiments. A weak probe beam (< 0.5 mW cm^{-2}) from the other single-frequency laser was tuned to the same D-line resonance. The probe beam was chopped and copropagated with the strong pumping beam through the sodium oven. The probe-beam frequency was tuned over the Doppler-broadened resonance for a fixed tuning of the strong beam and the absorption of the probe beam was measured with a phase-sensitive detector. The absorption results shown in Fig. 11

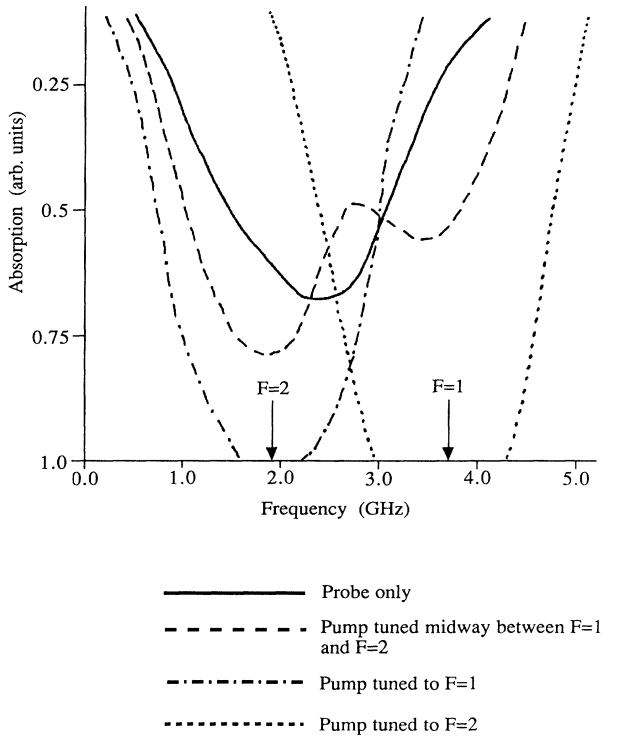

FIG. 11. Measured absorption of a probe beam on the $3S\rightarrow 3P_{3/2}$ transition for different pump tunings.

confirmed that the strong beam was producing very significant changes in the ground-state hyperfine population distribution. With the strong beam tuned onto one of the hyperfine transitions, most of the population was optically pumped into the other ground-state hyperfine level. The absorption lines remained Doppler broadened in spite of the single-frequency laser excitation due to the collisional-induced interaction with the whole inhomogeneous distribution [62–64]. No evidence of distortion in the two-photon line shapes due to velocity-selective optical pumping was observed due to the presence of the buffer gas [65]. In general, the detrimental effects of optical pumping were minimized when recording the incoherent fluorescence and coherent SFM line profiles by tuning the laser frequency ω_1 midway between the hyperfine transition frequencies of the $3S \rightarrow 3P$ single-photon transition. For nonoptimum tunings of ω_1 the optical-pumping effect with the intermediate $3P$ states on resonance produced variations in the measured spectroscopic line intensities and more importantly reduced the overall SFM signal strength through refractive index changes and further phase mismatching. These effects of optical pumping on the SFM line profiles are experimentally displayed in the next section. Similar but more complicated optical-pumping effects were also evident when the magnetic field was applied to the sodium oven.

3. *SFM line profiles*

The variation of the magnetic-field-induced SFM power with two-photon detuning was examined by holding laser frequency ω_1 at a fixed detuning from the center of the Doppler-broadened $3S_{1/2} \rightarrow 3P_{3/2}$ single-photon transition and scanning laser frequency ω_2 through the resonantly enhancing two-photon transitions to the sodium $4D$ states. The line profiles of the incoherent fluorescence at 330 nm, which monitored the population in the 4D states, and the coherent SFM emission at 289.4 nm were compared under the same experimental conditions.

In contrast to magnetic-field-induced SHG where the line shapes of the SHG and the cascade fluorescence closely followed each other, the coherent and incoherent line profiles for magnetic-field-induced SFM proved to be quite different. This was due to the frequency-dependent phase-matching effects on the SFM emission which became unavoidable when the $3P$ intermediate states were resonant in the two-photon excitation. Consider the experimental line profiles shown in Fig. 12, which were recorded with a small applied transverse magnetic field and using the resonant $3P_{3/2}$ state as the intermediate step in the two-photon transition. For this relatively simple case, the magnetic splittings of the ground, intermediate, and final states are less than the effective homogeneous width of $\approx$400 MHz, (FWHM), which is power and collisionally broadened, and the large number of individual hyperfine transitions are not resolved. Figure 12(a) shows the population line profile and displays the expected velocity-selective peaks. The peaks corresponding to resonance with the $4D_{3/2}$ and $4D_{5/2}$ final states are marked with arrows. The lower line profile [Fig. 12(b)] shows the corresponding magnetic-field-induced SFM

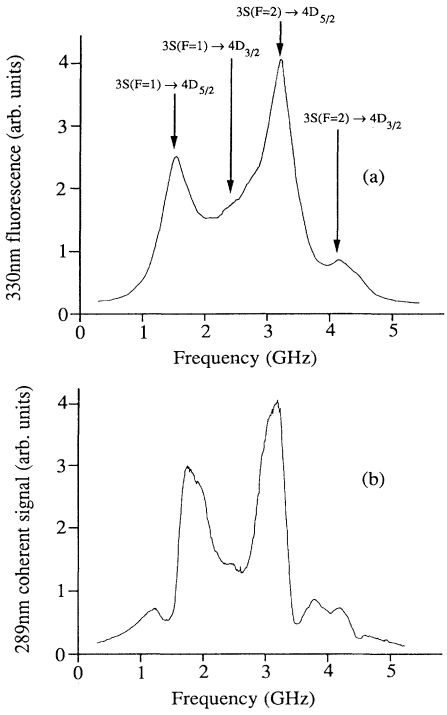

FIG. 12. Experimental line profiles for (a) 330-nm fluorescence and (b) 289-nm coherent SFM. Magnetic-field strength $=0.004$ T, vapor temperature $=393$ K, 1 mbar helium buffer gas, $I_1 = 240$ mW cm^{-2}—polarization perpendicular to the magnetic field, $I_2 = 875$ mW cm^{-2}—polarization perpendicular to the magnetic field. Laser frequency ν_1 tuned midway between the $3S_{1/2}(F=1) \rightarrow 3P_{3/2}$ and $3S_{1/2}(F=2) \rightarrow 3P_{3/2}$ single-photon transition frequencies.

coherent emission. The coherent line profile is different in that it now displays subhomogeneous features with apparent holes appearing in the measured SFM power due to the effect of phase matching on the nonlinear-optical effect. As discussed in Sec. II, the peak SFM emission also preferentially occurs for the velocity-selected homogeneous group but the total emitted power varies across the homogeneous line due to frequency-dependent refractive index changes for the fundamental waves and an ensuing phase mismatch. These effects were theoretically modeled in Fig. 5 and the experimental results are in reasonable qualitative agreement despite the simple three-level nature of the theoretical model.

The effects of optical pumping on the SFM line profile are shown in Fig. 13, where the single-photon detuning Δ_1 is varied by selecting different fixed values of ω_1. When ω_1 is not tuned to minimize the optical pumping as discussed in Sec. III B 2, there is a significant change in the ground-state population and a corresponding refractive index variation for ω_1. This refractive index change increases the overall phase mismatch and so less net SFM power is emitted, as is shown in the line profiles by the signal being reduced by over an order of magnitude when ω_1 is not optimally tuned. The emitted SFM power is less

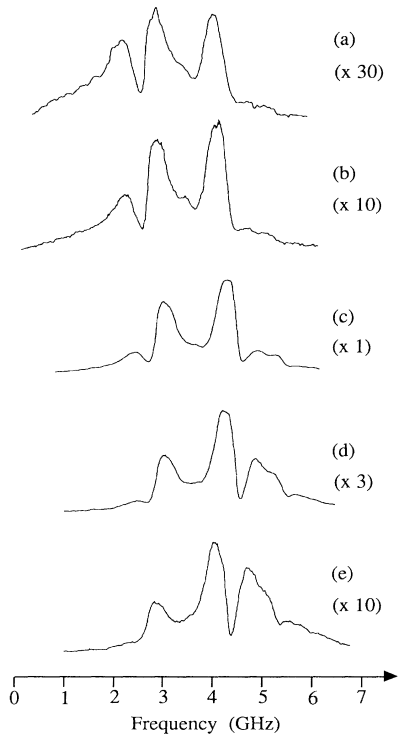

FIG. 13. Experimental SFM line profiles for ν_1 frequencies of (a) $3S_{1/2}(F=1)\rightarrow 3P_{3/2}$, (b) $3S_{1/2}(F=1)\rightarrow 3P_{3/2}-0.25$ GHz, (c) midway between the $3S_{1/2}(F=1)\rightarrow 3P_{3/2}$ and $3S_{1/2}(F=2)\rightarrow 3P_{3/2}$ transitions, (d) $3S_{1/2}(F=2)\rightarrow 3P_{3/2}+0.25$ GHz, (e) $3S_{1/2}(F=2)\rightarrow 3P_{3/2}$. The vertical axis for each line profile is the SFM power in arbitrary units. Other experimental parameters as in Fig. 12.

when the $F=2$ rather than $F=1$ ground-state level is populated by optical pumping because transitions from the $F=2$ ground-state level have larger oscillator strengths and produce a correspondingly larger phase mismatch. The homogeneous phase-matching effects are still more apparent for the transitions originating from the depleted ground-state hyperfine level because the optical pumping is not 100% efficient and this level retains a larger velocity-selected homogeneous population than the pumped ground-state level.

A similar line-shape comparison with a larger magnetic-field strength applied to the sodium vapor and using the D_1 resonance for enhancement is shown in Fig. 14. This line shape is more complicated due to the increased number of resolved two-photon transitions, all with their individual Doppler shifts and absolute two-photon resonant frequencies. The SFM line profile again displays the homogeneous phase-matching behavior and the frequencies of the holes correspond to the frequencies of the peaks in the population line profile. There is also significant SFM power where the $4D$ population is relatively weak. This contribution to the nonlinear process is produced by those velocity-selected groups which are exactly single-photon resonant to give a large resonant enhancement to the $\chi^{(2)}$ nonlinearity but not two-photon

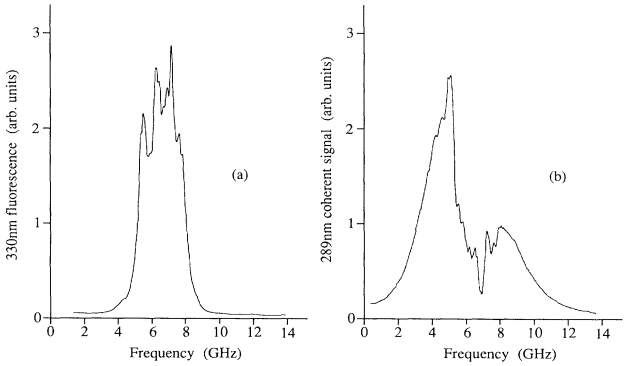

FIG. 14. Experimental line profiles for (a) 330-nm fluorescence and (b) 289-nm coherent SFM. Magnetic-field strength $=0.05$ T, 1 mbar argon buffer gas, vapor temperature $=393$ K, laser polarizations both perpendicular to the magnetic-field direction. Laser frequency ν_1 tuned midway between the $3S_{1/2}(F=1)\rightarrow 3P_{1/2}$ and $3S_{1/2}(F=2)\rightarrow 3P_{1/2}$ single-photon transition frequencies.

resonant with the $4D$ states to excite a significant population.

The magnetic-field-induced SFM line profiles were also affected by the vapor temperature and the buffer gas pressure. Increasing the sodium density via the vapor temperature generally led to an increase in the total SFM power, which was not continually dependent on the square of the number density but displayed the associated oscillatory phase-matching behavior. The magnitude of the homogeneous phase-matching effects was also enhanced at higher sodium particle densities as expected for a macroscopic response of the nonlinear medium. Larger pressures (≈ 10 mbar) of buffer gas added to the sodium oven reduced the overall SFM power through collisional dephasing of the coherence, and the Doppler-free line-shape features were no longer resolved due to further collisional broadening of the homogeneous linewidths.

4. Single- and two-photon saturation

The laser power dependence of both the coherent SFM radiation and the incoherent cascade fluorescence become nonlinear when ω_1 is tuned on resonance within the single-photon transition Doppler width. The measured intensity variations of the 330-nm fluorescence and the 289.4-nm coherent SFM emission with laser power at frequencies ω_1 and ω_2 both show marked saturations in the microscopic response since in general the individual laser intensities exceed the theoretical single-photon saturation intensities and there is additional two-photon saturation [66,67]. The degree of the two-photon saturation is difficult to estimate because the normal perturbative approximations are not valid in this case where the intermediate states in the two-photon absorption are resonant [68]. The intensity of the 330-nm fluorescence, which is proportional to the population in the final $4D$ sodium states, appears to approximately vary as the square root of the laser power at frequency ω_2, which is expected for

a saturated inhomogeneously broadened transition [47]. The intensity variation with the laser power at ω_1 is similar but there is an additional reduction in the fluorescence intensity with decreasing laser power, which is probably due to absorption over a shorter length in the sodium oven. The SFM intensity behavior with laser power is more complicated due to the phase-matching considerations. The dependence of the SFM power on the laser power at ω_2 is no longer proportional to $[I(\omega_2)]^{1/2}$ and the dependence on the laser power at ω_1 shows a marked decrease with decreasing power, also due to a shorter effective interaction length for the nonlinear-optical effect. These saturation effects also act to limit the obtainable magnetic-field-induced SFM output power with the intermediate states on resonance, in addition to the macroscopic phase-matching effects, and must be minimized to increase the overall conversion efficiency.

C. Improved conversion efficiency

The power conversion efficiency of the magnetic-field-induced SFM nonlinear-optical process was very low ($\approx 10^{-11}$) under the experimental conditions described in the preceding section. However, the conversion efficiency was increased by several orders of magnitude through optimization of the sodium atomic density, the input beam intensities, the magnetic-field strength, and the single- and two-photon detunings.

The intensity of the incident laser light was increased by focusing both fundamental beams collinearly into the oven to a spot size of 200 μm. This increased the intensity of each beam by ≈ 400 times and gave a confocal parameter for the Gaussian beams that was approximately equal to the length of the sodium vapor zone.

The sodium density was increased from $\approx 10^{11}$ to $\approx 10^{13}$ cm^{-3}, which should have increased the SFM power by a factor of 10^6 for all other parameters being fixed. However, as the sodium vapor density was increased the linear absorption of the laser beam at frequency ω_1 tuned near the $3S \rightarrow 3P$ single-photon transition frequency became extremely high and all of this beam was absorbed in the first few millimeters of the oven, so that the effective interaction length for the nonlinear process was greatly decreased.

Increasing the strength of the transverse magnetic field to a large value of ≈ 0.4 T produced beneficial effects for the linear absorption and dispersion of the sodium vapor. The $\Delta m_J = \pm 1$ $3S_{1/2} \rightarrow 3P_{3/2}$ transition frequencies were symmetrically split by several Doppler widths for this large magnetic-field strength and the residual linear absorption for light polarized perpendicular to the magnetic-field direction and tuned midway between these transitions was greatly reduced. This allowed the effective interaction length to be increased from a few millimeters at low magnetic-field strengths to approximately half the length of the oven. For a 10-cm oven length, a 0.4-T magnetic field, and a sodium density of $\approx 2 \times 10^{13}$ cm^{-3}, we experimentally measured the linear absorption coefficient to be $\alpha \approx 0.22$ cm^{-1} at the peak of the transmission near the midpoint frequency of the $\Delta m_J = \pm 1$ sodium transitions. The main contributions to the refractive index of the sodium vapor were also due to the same magnetically split single-photon transitions, and close to the midpoint frequency there were cancellation effects in the dispersion arising from each group of allowed sodium transitions. This allowed phase matching to be maintained by having a relatively low and controllable refractive index for the beam at frequency ω_1 by tuning near the midpoint frequency. At this frequency there is significant single-photon resonant enhancement ($\Delta_1 \approx 7$ GHz) but ω_1 lies outside the single-photon Doppler width so that the SFM is entirely an inhomogeneous process and the laser powers do not exceed the saturation intensities.

With the experimental parameters $N = 2 \times 10^{13}$ cm^{-3}, $B = 0.4$ T, $P(\omega_1) = 170$ mW, $P(\omega_2) = 210$ mW, ω_1 tuned between the magnetically split $3S_{1/2} \rightarrow 3P_{3/2}$ transitions and ω_2 tuned onto two-photon resonance with the $4D$ states, a maximum coherent SFM power of 4.6 μW was generated. This corresponded to a power conversion efficiency of 1.2×10^{-5} in spite of the use of a weak quadrupole transition in the excitation scheme. This cw conversion efficiency compared favorably with the 3×10^{-4} energy conversion efficiency previously obtained in electric-field-induced SFM with higher-power pulsed lasers and using only dipole transitions in the atomic excitation route [7].

For fixed ω_1, tuning ω_2 through the two-photon resonance produces two Doppler-broadened peaks (FWHM ≈ 4.5 GHz) separated by ≈ 25 GHz, which arise from the two groups of $\Delta m = \pm 2$ quadrupole transitions that resonantly enhance the SFM emission when the laser polarizations are perpendicular to the magnetic-field direction. However, for fixed ω_2 tuning ω_1 by only ≈ 200 MHz completely eliminates the SFM signal, which is indicative of a critical frequency-dependent phase-matching condition being achieved on the single-photon D-line transition. Maximizing the overall SFM power requires careful optimization of the laser frequencies, the sodium density, and the magnetic-field strength.

IV. CONCLUSIONS

We have experimentally and theoretically studied magnetic-field-induced SFM and the role of the intermediate states in the nonlinear-optical process. With the intermediate states nonresonant, the microscopic behavior was similar to SHG but the macroscopic response was modified due to the ability to select the sign and magnitude of the phase mismatch with the appropriate single-photon laser detuning. Phase-shifting effects due to the focused laser beams were observed in the SFM phase matching, which agreed well with the theoretically expected behavior. The optimum phase-match conditions were realized so that the SFM power continually increased with the sodium particle density.

Bringing the intermediate states onto resonance significantly altered the SFM behavior. The two-photon excitation and SFM nonlinear process became velocity selective due to hole burning in the single-photon Doppler width and homogeneous features were resolved in the line profiles. The SFM output power was modulat-

ed across the line profile due to homogeneous refractive index variations and ensuing phase mismatching. Our simple theoretical three-level model successfully accounted for this interplay of microscopic and macroscopic effects. Additional complications in interpreting the line profiles arose due to frequency-selective optical pumping in the $3S_{1/2}$ ground state.

Careful control over these experimental conditions allowed the SFM conversion efficiency to be increased by many orders of magnitude. The conversion efficiency could potentially be increased much further by utilizing more favorable atomic transitions and higher-power excitation.

ACKNOWLEDGMENTS

One of us (A.J.P.) gratefully acknowledges personal financial support from The Carnegie Trust for the Universities of Scotland. We thank British Aerospace, Filton, for the loan of equipment.

---

*Present address: BT Laboratories, Martlesham Heath, Ipswich, IP5 7RE, United Kingdom. FAX: (0473) 637593.

†FAX: (0334) 74487.

[1] N. Bloembergen, *Nonlinear Optics* (Benjamin, New York, 1965).

[2] S. Kielich, IEEE J. Quantum Electron. **QE-5**, 562 (1969).

[3] R. S. Finn and J. F. Ward, Phys. Rev. Lett. **26**, 285 (1971).

[4] I. J. Bigio, R. S. Finn, and J. F. Ward, Appl. Opt. **14**, 336 (1975).

[5] D. P. Shelton and A. D. Buckingham, Phys. Rev. A **26**, 2787 (1982).

[6] R. W. Boyd and L. Xiang, IEEE J. Quantum Electron. **QE-18**, 1242 (1982).

[7] D. J. Gauthier, J. Krasinski, and R. W. Boyd, Opt. Lett. **8**, 211 (1983).

[8] R. W. Boyd, D. J. Gauthier, J. Krasinski, and M. S. Malcuit, IEEE J. Quantum Electron. **QE-20**, 1074 (1984).

[9] D. P. Shelton and V. Mizrahi, Phys. Rev. A **33**, 72 (1986).

[10] A. Flusberg, T. Mossberg, and S. R. Hartmann, Phys. Rev. Lett. **38**, 59 (1977).

[11] A. Flusberg, T. Mossberg, and S. R. Hartmann, Phys. Rev. Lett. **38**, 694 (1977).

[12] T. Mossberg, A. Flusberg, and S. R. Hartmann, Opt. Commun. **25**, 121 (1978).

[13] D. S. Bethune, R. W. Smith, and Y. R. Shen, Phys. Rev. A **17**, 277 (1978).

[14] A. Flusberg, T. Mossberg, and S. R. Hartmann, in *Coherence and Quantum Optics IV*, edited by L. Mandel and E. Wolf (Plenum, New York, 1978).

[15] M. Matsuoka, H. Nakatsuka, H. Uchiki, and M. Mitsunaga, Phys. Rev. Lett. **38**, 894 (1977).

[16] H. Uchiki, H. Nakatsuka, and M. Matsuoka, Opt. Commun. **30**, 345 (1979).

[17] M. H. Dunn, Opt. Commun. **45**, 346 (1983).

[18] H. Uchiki, H. Nakatsuka, and M. Matsuoka, J. Phys. Soc. Jpn. **52**, 3010 (1983).

[19] B. D. Sinclair and M. H. Dunn, Phys. Rev. A **34**, 3989 (1986).

[20] B. D. Sinclair and M. H. Dunn, J. Mod. Opt. **35**, 517 (1988).

[21] K. Miyazaki, T. Sato, and H. Kashiwagi, Phys. Rev. Lett. **43**, 1154 (1979).

[22] D. S. Bethune, Phys. Rev. A **23**, 3139 (1981).

[23] J. Okada, Y. Fukuda, and M. Matsuoka, J. Phys. Soc. Jpn. **50**, 1301 (1981).

[24] V. G. Arkhipkin, N. P. Makarov, A. K. Popov, V. P. Timofeev, and V. Sh. Epshtein, Kvant. Elektron. (Moscow) **8**, 1104 (1981) [Sov. J. Quantum Electron. **11**, 656 (1981)].

[25] K. Miyazaki, T. Sato, and H. Kashiwagi, Phys. Rev. A **23**, 1358 (1981).

[26] W. Jamroz, P. E. LaRocque, and B. P. Stoicheff, Opt. Lett. **7**, 148 (1982).

[27] V. Mizrahi and D. P. Shelton, Phys. Rev. A **33**, 1396 (1986).

[28] S. G. Dinev, J. Phys. B **21**, 1111 (1988).

[29] S. Dinev, J. Phys. B **21**, 1681 (1988).

[30] D. S. Bethune, R. W. Smith, and Y. R. Shen, Phys. Rev. Lett. **37**, 431 (1976).

[31] D. S. Bethune, R. W. Smith, and Y. R. Shen, Phys. Rev. Lett. **38**, 647 (1977).

[32] D. S. Bethune, R. W. Smith, and Y. R. Shen, in *Coherence and Quantum Optics IV* (Ref. [14]).

[33] D. S. Bethune, Opt. Lett. **6**, 287 (1981).

[34] J. E. Bjorkholm and P. F. Liao, Phys. Rev. Lett. **33**, 128 (1974).

[35] J. E. Bjorkholm and P. F. Liao, IEEE J. Quantum Electron. **QE-10**, 906 (1974).

[36] J. E. Bjorkholm and P. F. Liao, Phys. Rev. A **14**, 751 (1976).

[37] P. F. Liao and J. E. Bjorkholm, Phys. Rev. Lett. **36**, 1543 (1976).

[38] P. F. Liao, J. E. Bjorkholm, and P. R. Berman, Phys. Rev. A **20**, 1489 (1979).

[39] P. F. Liao, J. E. Bjorkholm, and P. R. Berman, Phys. Rev. A **21**, 1927 (1980).

[40] R. G. Brewer and E. L. Hahn, Phys. Rev. A **11**, 1641 (1975).

[41] R. M. Whitley and C. R. Stroud, Jr., Phys. Rev. A **14**, 1498 (1976).

[42] R. Salomaa and S. Stenholm, J. Phys. B **8**, 1795 (1975).

[43] R. Salomaa and S. Stenholm, J. Phys. B **9**, 1221 (1976).

[44] M. S. Feld and A. Javan, Phys. Rev. **177**, 540 (1969).

[45] V. S. Letokov and V. P. Chebotayev, *Nonlinear Laser Spectroscopy* (Springer-Verlag, Berlin, 1977).

[46] N. Bloembergen and M. D. Levenson, in *High Resolution Laser Spectroscopy*, edited by K. Shimoda, Topics in Applied Physics Vol. 13 (Springer-Verlag, Berlin, 1976), p. 315.

[47] A. Yariv, *Quantum Electronics*, 3rd ed. (Wiley, New York, 1989).

[48] P. R. Berman, Phys. Rep. **43C**, 101 (1978).

[49] P. F. Liao and G. C. Bjorklund, Phys. Rev. Lett. **36**, 584 (1976).

[50] P. F. Liao and G. C. Bjorklund, Phys. Rev. A **15**, 2009 (1977).

[51] M. D. Levenson, *Introduction to Nonlinear Laser Spectros-*

copy (Academic, New York, 1982).
[52] T. Hansch and P. Toschek, Z. Phys. **236**, 373 (1970).
[53] A. Yariv, *Introduction to Optical Electronics,* 3rd ed. (Holt-Saunders, Tokyo, 1985).
[54] D. C. Hanna, M. A. Yuratich, and D. Cotter, *Nonlinear Optics of Free Atoms and Molecules* (Springer-Verlag, Berlin, 1979).
[55] J. A. Armstrong, N. Bloembergen, J. Ducuing, and P. S. Perhan, Phys. Rev. **127**, 1918 (1962).
[56] G. C. Bjorklund, J. E. Bjorkholm, P. F. Liao, and R. H. Storz, Appl. Phys. Lett. **29**, 729 (1976).
[57] G. C. Bjorklund, J. E. Bjorkholm, R. R. Freeman, and P. F. Liao, Appl. Phys. Lett. **31**, 330 (1977).
[58] S. E. Harris and R. B. Miles, Appl. Phys. Lett. **19**, 385 (1971).
[59] D. A. Kleinman, A. Ashkin, and G. D. Boyd, Phys. Rev. **145**, 338 (1966).
[60] G. D. Boyd and D. A. Kleinman, J. Appl. Phys. **39**, 3597 (1968).
[61] W. Happer, Rev. Mod. Phys. **44**, 169 (1972).
[62] R. Walkup, A. Spielfiedel, W. D. Phillips, and D. E. Pritchard, Phys. Rev. A **23**, 1869 (1981).
[63] P. G. Pappas, R. A. Forber, W. W. Quivers, Jr., R. R. Dasari, M. S. Feld, and D. E. Murnick, Phys. Rev. Lett. **47**, 236 (1981).
[64] W. W. Quivers, Jr., R. A. Forber, A. P. Ghosh, D. J. Heinzen, G. Shimkaveg, M. A. Attili, C. Stubbins, P. G. Pappas, R. R. Dasari, M. S. Feld, Y. Niv, and D. E. Murnick, in *Laser Spectroscopy V,* edited by A. R. W. McKellar, T. Oka, and B. P. Stoicheff, Springer Series in Optical Science Vol. 30 (Springer-Verlag, Berlin, 1981), p. 186.
[65] J. E. Bjorkholm, P. F. Liao, and A. Wokaun, Phys. Rev. A **26**, 2643 (1982).
[66] C. C. Wang and L. I. Davis, Jr., Phys. Rev. Lett. **35**, 650 (1975).
[67] J. F. Ward and A. V. Smith, Phys. Rev. Lett. **35**, 653 (1975).
[68] G. Grynberg, B. Cagnac, and F. Biraben, in *Coherent Nonlinear Optics—Recent Advances,* edited by M. S. Feld and V. S. Letokhov, Topics in Current Physics Vol. 21 (Springer-Verlag, Berlin, 1980), p. 111.